Hard x-ray photoemission study of near-Heusler Fe_xSi_{1-x} alloys

A. X. Gray,[1,2] J. Karel,[3] J. Minár,[4] C. Bordel,[5,6] H. Ebert,[4] J. Braun,[4] S. Ueda,[7] Y. Yamashita,[7] L. Ouyang,[8] D. J. Smith,[8] K. Kobayashi,[7] F. Hellman,[2,3,5] and C. S. Fadley[1,2]

[1]*Department of Physics, University of California, Davis, California 95616, USA*

[2]*Materials Sciences Division, Lawrence Berkeley National Laboratory, Berkeley, California 94720, USA*

[3]*Department of Materials Science and Engineering, University of California Berkeley, Berkeley, California 94720, USA*

[4]*Dept. Chemie und Biochemie, Physikalische Chemie, Universität München, Butenandtstrasse 5-13, 81377 München, Germany*

[5]*Department of Physics, University of California Berkeley, Berkeley, California 94720, USA*

[6]*Groupe de Physique des Matériaux, UMR CNRS 6634, Université-INSA de Rouen, Avenue de l'Université - BP12, 76801 Saint Etienne du Rouvray, France*

[7]*NIMS Beamline Station at SPring-8, National Institute for Materials Science, Sayo, Hyogo 679-5198, Japan*

[8]*Department of Physics, Arizona State University, Tempe, Arizona 85287, USA*

(Received 15 February 2011; published 9 May 2011)

The structural and electronic properties of epitaxial and amorphous Fe_xSi_{1-x} alloys with $x = 0.72$ and 0.67 near the binary Heusler composition of $x = 0.75$ were determined using hard x-ray photoelectron spectroscopy (HXPS). By performing the measurements at a photon energy of 5950.3 eV, the bulk-sensitivity of the measurement is enhanced by a factor of 4–7 compared to conventional soft x-ray photoelectron spectroscopy at about 1000 keV. HXPS probes, on average, as far as 76 Å into the Fe_xSi_{1-x} samples. Via core-level spectra, it is found in the amorphous alloy that, in spite of the disordered structure that could lead to a broad distribution of chemical environments, the Si environment is mostly unique. Valence-band spectra reveal a clear distinction between the contributions of the two inequivalent Fe sites of the most highly ordered ($x = 0.72$, $D0_3$) epitaxial sample. The valence-band spectra are compared to results of fully relativistic coherent potential approximation calculations performed in the framework of the one-step model of photoemission, which reveal details of the atomic-orbital makeup of various features, and generally exhibit good agreement with experiment.

DOI: 10.1103/PhysRevB.83.195112 PACS number(s): 79.60.Dp, 71.20.Be, 71.20.Eh, 71.20.Gj

I. INTRODUCTION

Ferromagnetic Fe_3Si has attracted significant interest due to its potential as a spin injector into semiconductors.[1,2] This stoichiometric compound can be viewed as Fe_2FeSi, which is a binary Heusler alloy having two different Fe sites[3] with different moments. It was theoretically predicted to have a significant spin polarization at the Fermi energy, due to the splitting in energy of the majority- and minority-spin channels,[4,5] but the experimentally observed degree of spin polarization remains low, which is an obstacle for spintronics applications.[6] Up to now, significant work has been devoted to Fe_3Si,[1,2,6–9] but very little is known about nonstoichiometric alloys[10] or amorphous alloys.[11] In the composition range $0.55 < x < 0.75$, a two-phase region of the bulk equilibrium phase diagram, thin-film growth can be used to produce homogeneous alloys with varying degrees of structural and chemical ordering. This ordering affects the physical properties of the material, including, in particular, the electrical resistivity and magnetic properties, which can be significantly tuned.

The $D0_3$ crystal structure is the equilibrium structure of stoichiometric Fe_3Si. The unit cell has an fcc Bravais lattice and can be thought of as eight bcc-like subunits with Fe on the cube corners (Fe_{II}), and Fe (Fe_I) and Si alternating in the body centers.[12] In this structure, Fe_{II} have four-nearest-neighbor Fe and four-nearest-neighbor Si, while Fe_I have eight-nearest-neighbor Fe. In epitaxial samples with off-stoichiometric compositions ($0.55 < x < 0.75$), three different chemical orderings are possible. The additional Si can preferentially substitute for Fe in the body-centered (Fe_I) positions to maintain a $D0_3$ ordered structure,[12,13] causing a decreased number of Fe_I and a decrease in the ratio of Fe/Si neighbors for Fe_{II}. The alloy can also form in the closely related $B2$ (CsCl) structure, which at $x = 0.5$ has Fe on cube corners and Si in the body centers, with all Fe atoms surrounded by Si; this structure has distinct symmetry, but could be thought of as the limit of $D0_3$ where the number of Fe_I *and* the ratio of Fe/Si neighbors for Fe_{II} have both gone to zero. For x between 0.5 and 0.75, there is, however, an important distinction between $D0_3$ and $B2$, which lies in whether Fe_I and Si in the body-centered positions are randomly arranged or preserve a long-range alternating structure with occasional substitution of Si at Fe_I sites. For the same composition, both structures have the same nearest-neighbor arrangements for all body centers (all Si and Fe_I atoms are surrounded by eight Fe atoms), but the next nearest neighbors (which are important for both magnetic and electronic properties) are different. The Fe_{II} atoms statistically have the same average neighbor ratio, but the width of the distribution is much wider for $B2$ than $D0_3$. The third possibility is an $A2$ structure, which is a random bcc solid solution with Fe and Si randomly occupying both corner and body-centered positions. The last possibility is a structurally disordered amorphous material. These differences in chemical and structural ordering produce different magnetic and electrical properties. The aim of this study is to investigate the role of composition as well as structural and chemical ordering on the electronic properties of homogeneous metastable Fe_xSi_{1-x} samples.

For this study, we used hard x-ray photoelectron spectroscopy (HXPS) to measure core and valence electronic levels for three samples—epitaxial $Fe_{0.72}Si_{0.28}$ (epi-$Fe_{0.72}Si_{0.28}$),

epitaxial $Fe_{0.67}Si_{0.33}$ (epi-$Fe_{0.67}Si_{0.33}$), and amorphous (with some nanocrystals) $Fe_{0.67}Si_{0.33}$ (a-$Fe_{0.67}Si_{0.33}$)—to investigate the differences in structural and electronic properties of these alloys as a function of composition and degree of crystallinity. The first sample (epi-$Fe_{0.72}Si_{0.28}$) was chosen because $x = 0.72$ is close to the Fe content of the stoichiometric alloy, so we expect a high degree of chemical order in addition to the structural order. The second one (epi-$Fe_{0.67}Si_{0.33}$) was selected to study the effect of composition but not structural disorder, and the last one (a-$Fe_{0.67}Si_{0.33}$) to investigate the combined effects of composition and structural disorder on the electronic structure of these alloys.

X-ray photoelectron spectroscopy (XPS) has been used extensively to study chemical and electronic properties of Heusler alloys.[14–16] However, due to the low inelastic mean-free path (IMFP) of the photoemitted electrons with kinetic energies ranging typically from a few hundred to 1000 eV, conventional soft x-ray photoelectron spectroscopy measurements are inherently surface-sensitive. This may result in spectra that are dominated by surface effects, such as roughness, surface reconstruction, native oxides, and contaminant layers, a serious deficiency if the bulk properties of the sample are of interest. According to the widely used TPP-2M formula, which enables us to estimate the IMFP values for most solids,[17,18] by performing photoemission measurements in the hard x-ray regime, in our particular case with an excitation energy of 5950.3 eV, we increase the IMFP of valence electrons by a factor of 4–7 for $Fe_{0.72}Si_{0.28}$, with the IMFP of 76 Å, as compared to IMFP's of 11–18 Å in the soft x-ray regime (500–1000 eV).

As discussed in more detail below, the shapes and positions of Si (1s and 2p) and Fe (2p and 3s) core levels were investigated. Detailed analyses of the O 1s and C 1s core peaks were also performed to determine the composition and amount of native oxide and a carbon-containing atmospheric contaminant layer found on the surface. Finally, analysis of the valence-band spectra, dominated by Fe 3d and Si 3s contributions at this high energy, revealed significant differences between the alloys of the two compositions and structural orderings. Several prior XPS studies have investigated the valence levels of iron silicides;[19–21] however, most of them concentrate on the low-binding-energy region of 10–12 eV below the Fermi level. In contrast, we have performed our measurements in the hard x-ray regime so as to look four to seven times deeper into the bulk, and we have also examined a wider binding-energy range of 40 eV below the Fermi level. Comparing our data to one-step photoemission theory[22,23] provides significant further insight concerning the valence spectra, as discussed below.

II. SAMPLE PREPARATION

All films were prepared by electron beam coevaporation of Fe and Si at base pressures below 9.0×10^{-9} Torr. The epitaxial samples were grown on MgO (001) at 300 °C, and the amorphous sample was grown on amorphous SiN_x deposited on a Si substrate at room temperature. All samples were approximately 2000 Å thick, and the growth rate for Fe was fixed at 0.35 Å/s. The Si growth rate was varied to obtain the desired composition. Compositions were measured using Rutherford backscattering spectrometry (RBS), and film thicknesses were determined with a KLA Tencor Alpha Step IQ profilometer. Compositions were also confirmed by analyzing HXPS core-photoelectron relative peak intensities.

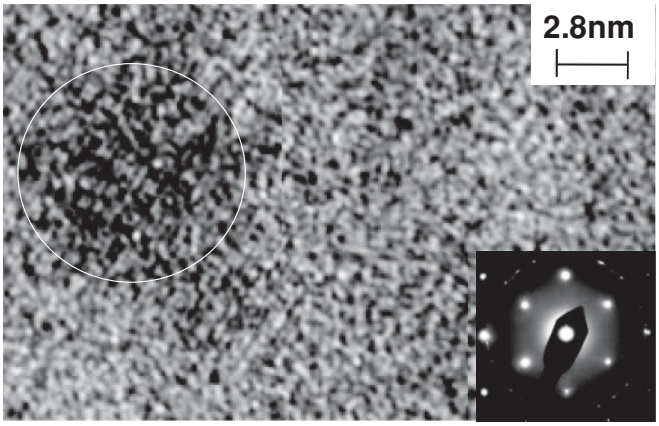

FIG. 1. TEM image and electron diffraction pattern (inset) for the amorphous film $x = 0.67$, designated as a-$Fe_{0.67}Si_{0.33}$. The image displays an ~5 nm diam nanocrystal (circled) in an amorphous matrix, which is estimated to represent ~80% of the sample surface area. In addition to strong spots from the ⟨110⟩-oriented Si substrate, the electron diffraction pattern shows a broad diffuse ring originating from the amorphous film, as well as some random spots from nanocrystals.

The atomic structure of the films was verified using transmission electron microscopy (a-$Fe_{0.67}Si_{0.33}$) and x-ray diffraction techniques (epi-$Fe_{0.72}Si_{0.28}$ and epi-$Fe_{0.67}Si_{0.33}$). Figure 1 shows a transmission electron microscope (TEM) image for a-$Fe_{0.67}Si_{0.33}$. This image shows a predominantly amorphous structure with some nanocrystals on the order of 5 nm in size embedded in it. The electron diffraction pattern (inset) displays sharp diffraction spots from the Si substrate and a broad diffraction ring with some weak spots, further indicating partial crystallinity. The volume fraction of the amorphous matrix is estimated from these images to be on the order of 80%, with ~20% representing nanocrystalline areas.

Figure 2(a) shows the θ-2θ x-ray diffraction patterns obtained from the epitaxial films. The superlattice [i.e., (200) $D0_3$ and (100) $B2$] and fundamental [i.e., (400) $D0_3$ and (200) $B2$] reflections referenced to the $A2$ structure are present at $2\theta = 31.8°$ ($x = 0.72$) and 32.1° ($x = 0.67$); and $2\theta = 66.4°$ ($x = 0.72$) and $2\theta = 67.0°$ ($x = 0.67$), respectively, with a small shift between the two curves. The observed superlattice peak in the θ-2θ x-ray diffraction patterns indicates chemical ordering in these films. However, from these data alone, it is not possible to discern whether the film structures are the $D0_3$ or $B2$ phases, since both would give rise to this superlattice peak. Conversion electron Mössbauer spectrometry (CEMS) on these samples provides the local chemical environments of the Fe atoms in the films. From these data, we find that the $x = 0.72$ sample is $D0_3$ while the $x = 0.67$ is $B2$. The lattice constants were calculated to be 5.63 and 2.79 Å for $x = 0.72$ [from the $D0_3$ (200) peak] and $x = 0.67$ [from the $B2$ (100) peak] respectively, and no other peaks are present, indicating a single out-of-plane orientation in the films. To confirm epitaxy,

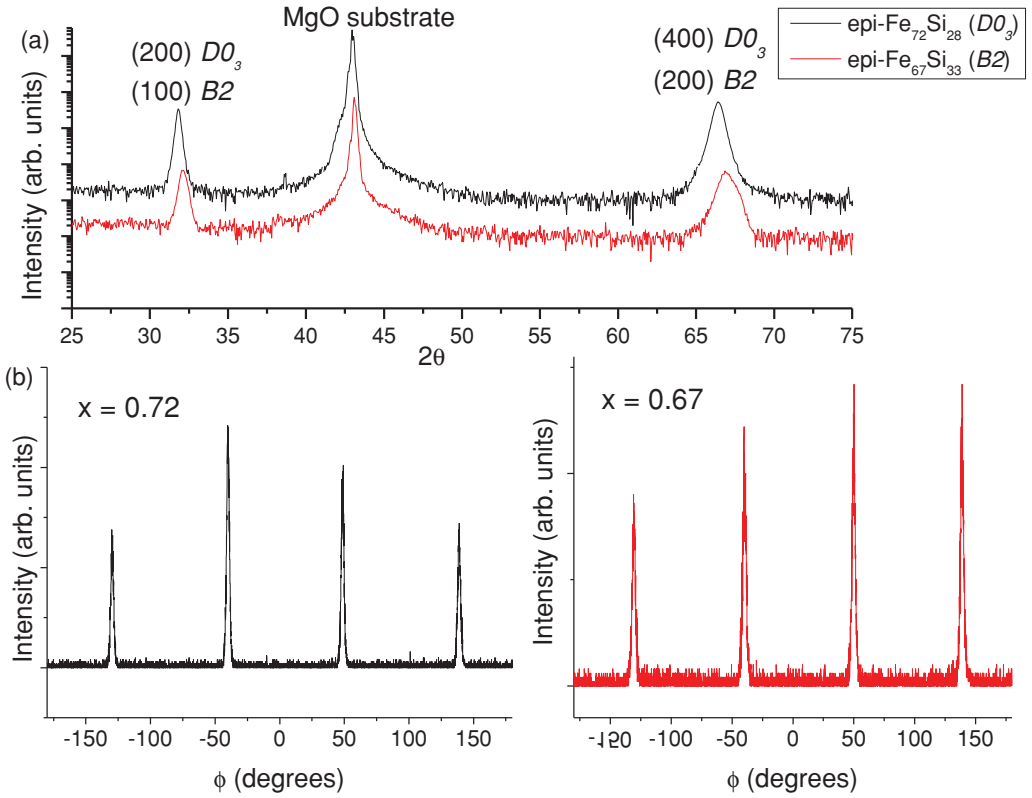

FIG. 2. (Color online) X-ray diffraction patterns for epitaxial samples designated as epi-$Fe_{0.72}Si_{0.28}$ and epi-$Fe_{0.67}Si_{0.33}$. (a) θ-2θ scans for $x = 0.72$ (black) and $x = 0.67$ (red) epitaxial films. (b) ϕ scans on the in-plane (220) peak for $x = 0.72$ (black) and the (110) peak for $x = 0.67$ (red); fourfold symmetry is observed, confirming epitaxy.

azimuthal (ϕ) scans were performed on the in-plane $\{110\}$ peak. Figure 2(b) shows the ϕ scans from these films; fourfold symmetry was observed, confirming an epitaxial film in both cases. The films are oriented [100] out-of-plane and rotated 45° in plane with respect to the MgO substrate, i.e., Fe_xSi_{1-x} [100]‖MgO [110].

III. EXPERIMENTAL METHOD

Hard x-ray photoemission measurements for this study were performed at the national synchrotron radiation facility SPring-8 in Japan, using undulator beamline BL15XU. The photon energy was set at 5950.3 eV, which is the energy yielding optimal resolution and flux for that particular beamline. The exciting radiation was incident on the sample at a grazing angle of 2.0° as measured from the sample surface plane, and the kinetic energies of the photoemitted electrons were analyzed by a VG Scienta R4000 hemispherical analyzer oriented at an angle of 90° from the direction of the incoming x rays. The radiation is linearly polarized, with the polarization vector pointing in the direction of the analyzer. The electron takeoff angle as measured with respect to the surface is thus 88°, maximizing bulk sensitivity. In this measurement geometry, the x-ray attenuation length for $Fe_{0.72}Si_{0.28}$ is 4710 Å,[24] which ensures that the x rays penetrate deep into the bulk, well beyond the depths effective for electron emission. Some measurements were also done at a takeoff angle of 45° to vary the degree of surface versus bulk sensitivity. The overall energy resolution was set to 230 meV, and the absolute energy scale was checked frequently against the Au Fermi level, so that the energy positions in all spectra have an accuracy of ± 10 meV. The results of the HXPS measurements on core levels of all elements present, as well as the valence-band region, are presented in Figs. 3–5.

IV. MEASUREMENT RESULTS AND ANALYSIS

A. Core-level spectra

Figure 3(a) shows the Si 1s core-level spectra obtained for all three samples—epi-$Fe_{0.72}Si_{0.28}$ (black), epi-$Fe_{0.67}Si_{0.33}$ (red), and a-$Fe_{0.67}Si_{0.33}$ (blue). The spectra have had a Shirley background subtracted from them[25] and the heights have been normalized to the maxima. All three spectra show the presence of a chemically shifted oxide component at ∼1843 eV, but the shift is greater for the amorphous sample. No changes in the shape of the main elemental Si peak at a binding energy of ∼1839.5 eV are observed between the three samples; however, a chemical shift of 0.09 eV toward lower binding energy is observed for epi-$Fe_{0.67}Si_{0.33}$ relative to epi-$Fe_{0.72}Si_{0.28}$, and an even more prominent chemical shift of 0.31 eV toward lower binding energy is observed for the a-$Fe_{0.67}Si_{0.33}$ sample, relative to epi-$Fe_{0.67}Si_{0.33}$. These shifts occur because of the change in the chemical environment around the Si atoms in alloys of different compositions and/or different degrees of crystallinity. It is worth noting that the variation in crystallinity of the alloy affects the chemical state of the Si atoms more strongly than the change in the alloy

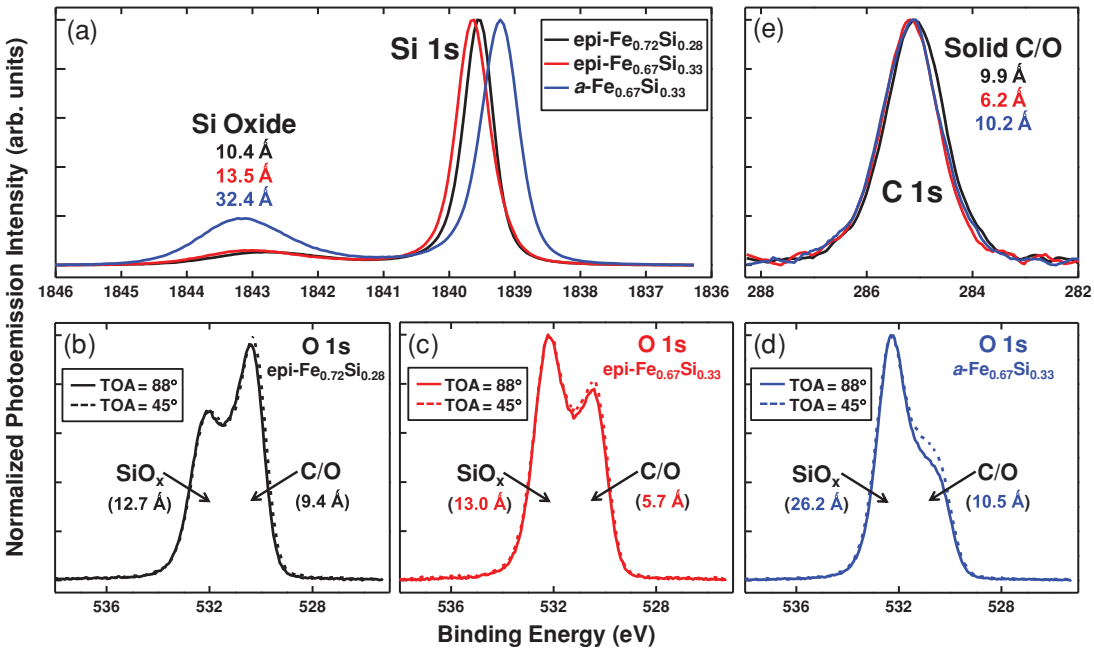

FIG. 3. (Color online) (a) Si 1*s* core peak spectra obtained for all three samples: epi-$Fe_{0.72}Si_{0.28}$, epi-$Fe_{0.67}Si_{0.33}$, and *a*-$Fe_{0.67}Si_{0.33}$. Two prominent features are the main Si 1*s* peak and the Si oxide peak. (b)–(d) O 1*s* peaks obtained for all three samples at the electron take-off angles (TOA) of 88° and 45°. The origins of the two components are identified to be the Si oxide layer and the solid C/O contaminant layer on the surface. (e) C 1*s* peaks, originating from the solid C/O contaminant layer on the surface, obtained for all three samples.

composition, i.e., the most significant chemical shift (0.31 eV) occurs between the epitaxial and amorphous alloys of similar composition ($Fe_{0.67}Si_{0.33}$). In addition, we do *not* observe significant disorder broadening for the amorphous film (only 0.1 eV broadening compared to a peak width of 0.7 eV and a shift of 0.31 eV), indicating that despite the amorphous structure, there is mostly a single chemical environment for Si in this film. A slight broadening is also visible in the Si 2*p* core levels, to be discussed below, which suggests the presence of other chemical states due to structural disorder.

As noted previously, the presence of some Si oxide is evident due to the observation of a second Si 1*s* oxide peak that is separated from the elemental peak by ∼3.3–3.9 eV.[26] This type of splitting, or chemical shift, occurs due to the difference in the chemical environments around Si atoms in an oxide compared to the Fe_xSi_{1-x} alloy, and has been observed in numerous studies (see, e.g., Refs. 26 and 27). The position of the oxide peak shifts by 0.09 eV toward lower binding energy for epi-$Fe_{0.67}Si_{0.33}$ relative to epi-$Fe_{0.78}Si_{0.22}$, which resembles the behavior of the main Si peak for these two alloys. The oxide peak for the *a*-$Fe_{0.67}Si_{0.33}$ sample, however, exhibits a very different behavior by shifting toward *higher* binding energy, by 0.44 eV, relative to the oxide peak for the epi-$Fe_{0.67}Si_{0.33}$ sample; the separation between the main peak and the oxide peak is 3.87 eV for the amorphous sample, compared to 3.27 eV for the epitaxial sample. These shift values, although slightly different in magnitude, are nevertheless consistent with results reported in prior studies of oxidized Si (see, e.g., Refs. 26 and 27). Similar behavior of elemental and oxide peaks is observed for the Si 2*p* peaks, and is discussed later in this paper. It is somewhat unusual that, for the amorphous sample, the oxide peak shifts to higher binding energy and the element peak to lower binding energy, thus increasing their separation. The oxide peak shift is understandable as the result of a greater degree of oxidation (higher oxidation state) in the amorphous sample. For the element peak, one might argue that final-state relaxation and screening of the core hole is easier in the amorphous state, thus lowering the binding energy. Similar effects between oxide and element have also been observed in polycrystalline silicon,[28] but no detailed theory is available.

It is also apparent in Fig. 3(a) that the intensity of the Si 1*s* oxide peak for the *a*-$Fe_{0.67}Si_{0.33}$ sample is much higher compared to the epitaxial sample, which suggests a more pronounced oxidation of silicon in the amorphous alloy. By looking at the ratio of the Si oxide peak intensity to the main Si 1*s* core peak intensity, and comparing it to the ratio predicted via a theoretical calculation, it is possible to estimate the thickness of the oxide. For this purpose, we used the NIST database program Simulation of Electron Spectra for Surface Analysis (SESSA),[29] which quantitatively predicts photoemission peak intensities by taking into account relevant parameters such as inelastic mean-free paths, elastic-scattering cross sections, photoionization asymmetry parameters, experimental geometry, etc. The ratios of the Si oxide peak intensity to the main Si 1*s* core peak intensity for epi-$Fe_{0.72}Si_{0.28}$, epi-$Fe_{0.67}Si_{0.33}$, and *a*-$Fe_{0.67}Si_{0.33}$ were estimated to be 1/6.6, 1/6.9, and 1/3.1, respectively. Assuming a single Si thin oxide overlayer, we obtain from these values the effective layer thicknesses for epi-$Fe_{0.72}Si_{0.28}$, epi-$Fe_{0.67}Si_{0.33}$, and *a*-$Fe_{0.67}Si_{0.33}$ of 10.4, 13.5, and 32.4 Å, respectively; there is thus about three times as much oxidation for the amorphous sample. Angle-resolved measurements between a takeoff angle of 88° and 45° with respect to the surface, in conjunction with

peak-intensity analyses, confirm that the oxide is localized at the surface of the samples.

A similar analysis can be performed by looking at the intensity of the O 1*s* core peak to estimate the thickness of native oxide in the sample, since one of the O 1*s* components originates from the presence of the Si oxide at the sample surface [Figs. 3(b)–3(d)]. In our case, the O 1*s* core peak has two prominent components separated by 1.55 eV and varying in relative intensities in the different samples. By quantitatively comparing the intensities of the two components individually to the intensities of the Si 1*s* oxide peak for each sample, we observe that the intensities of the higher-binding- energy component of the O 1*s* peak correlate with the intensities of the Si 1*s* oxide peak within ±7%. At the same time, there is no correlation between the intensity of the Si 1*s* oxide peak and the lower-binding-energy component of the O 1*s* peak. This result suggests that the higher-binding-energy component of the O 1*s* peak corresponds to the oxygen in the Si oxide, while the origin of the lower-binding-energy component is different; we will show below that its origin is a carbon-containing thin surface contamination layer.

As an alternate independent way of estimating the thickness of Si oxide, we looked at the intensity of the higher-binding-energy component of the O 1*s* peak and compared it to the intensity of the nearby Fe $2p_{3/2}$ peak, and we used the same experiment-to-SESSA theory intensity-ratio comparison as described earlier. The thicknesses of the Si oxide layers for epi-$Fe_{0.72}Si_{0.28}$, epi-$Fe_{0.67}Si_{0.33}$, and *a*-$Fe_{0.67}Si_{0.33}$ samples were thus estimated to be 12.7, 13.0, and 26.2 Å, respectively, which is very close (within 10%) to the values determined previously by comparing the intensities of the Si 1*s* element and oxide peaks. This consistency between the two sets of values obtained in two independent ways further confirms that the higher-binding-energy component of the O 1*s* peak corresponds to oxygen in a Si oxide, and further indicates relatively little Fe oxidation, a point to which we return below.

To determine the origin of the lower-binding-energy component of the O 1*s* peak, we measured O 1*s* spectra at two photoelectron take-off angles: 88° (solid line) and 45° (dashed line) as measured from the sample plane [Figs. 3(b)–3(d)]. By decreasing the take-off angle from 88° to 45°, we decrease the mean electron escape depth by a factor of 0.707 [sin(45°)/sin(88°)], thus significantly enhancing the surface sensitivity of the measurement. As we probe closer to the surface of the samples with a take-off angle of 45°, we observe an increase in the intensity of the lower-binding-energy component of the O 1*s* peak relative to the higher-binding-energy component for all three samples. Thus, we conclude that the lower-binding-energy component of the O 1*s* peak originates from an outermost oxygen-containing layer above the Si oxide. We further observe that the intensities of the lower-binding-energy components of the O 1*s* peak correlate to the intensities of the C 1*s* peak measured for each sample and displayed in Fig. 3(e), to within ±4%. The observed C 1*s* core peaks presumably arise due to the presence of thin carbon-containing contaminant layers on the surfaces of the samples. The correlation between C 1*s* and the lower-binding O 1*s* suggests that these contaminant layers also contain oxygen, e.g., CO. By comparing the C 1*s* core intensity to the intensity of a nearby Fe $2p_{3/2}$ core peak, it is further possible to estimate the thickness of the contaminant layer, again by using the SESSA simulation package. The thicknesses of the carbon-containing contaminant layers for epi-$Fe_{0.72}Si_{0.28}$, epi-$Fe_{0.67}Si_{0.33}$, and *a*-$Fe_{0.67}Si_{0.33}$ samples were estimated to be 9.9, 6.2, and 10.2 Å, respectively. To further verify that the lower-binding-energy components of the O 1*s* peaks originate from the solid contaminant layer, we compared their intensities to those of Fe $2p_{3/2}$ peaks, which we previously used as reference peaks, and obtained the solid contaminant thickness values of 9.4, 5.7, and 10.5 Å for epi-$Fe_{0.72}Si_{0.28}$, epi-$Fe_{0.67}Si_{0.33}$, and *a*-$Fe_{0.67}Si_{0.33}$ samples, respectively, which are consistent with the previous values to within ±4%. As a final aspect of this analysis, we can estimate the stoichiometry of the C- and O-containing surface contaminant layer to be $C_{1.0}O_{1.2}$.

The possible presence of any form of Fe oxide in the sample can be investigated by looking at the shapes and positions of the Fe 2*p* peaks shown in Fig. 4(a). Oxidation of Fe has been previously reported to be accompanied by significant changes in the shapes and binding energies of the Fe $2p_{1/2}$ and Fe $2p_{3/2}$ peaks.[30] Upon comparing our measurements to the prior results reported in Ref. 30, we observe that, apart from the difference in the peak width that arises due to the variation in the experimental resolution between the two studies, and the inelastic background intensity between the $p_{1/2}$ and $p_{3/2}$ peaks, our spectrum matches the Fe^0 spectrum, which leads to the conclusion that Fe in our Fe_xSi_{1-x} samples was not significantly oxidized [less than 5% (Ref. 30)]. This is consistent with the fact that the negative Gibbs free energy of oxide formation for SiO_2 (−824.9 kJ) is about twice as high as the values for FeO (−481.7 kJ), Fe_2O_3 (−414.5 kJ), or Fe_3O_4

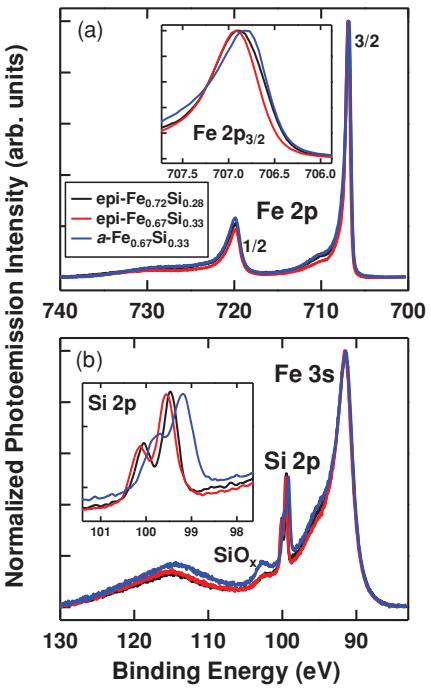

FIG. 4. (Color online) (a) Experimental Fe 2*p* spectra collected for all three samples, which do not exhibit any evidence of iron oxidation. (b) Fe 3*s* and Si 2*p* spectra obtained for all three samples. Fe 3*s* also does not show evidence of oxidation.

(−549.4 kJ),[31] and therefore SiO_2 is more likely to form from a thermodynamic standpoint, even though the kinetics of any surface oxidation reaction would also need to be considered.

We note that the Fe 2*p* peaks show small shifts to lower binding energy, on the order of 0.1 eV (see the inset). The direction of these shifts is consistent with that seen for the Si 1*s* element peak, but the magnitude of the shifts for Fe 2*p* peaks is about three times smaller than that for Si 1*s*. This can be qualitatively explained by the differences in atomic radii of Fe and Si atoms, with smaller atoms expected to show larger chemical shifts for a given change in valence charge or final-state screening.[32] The Fe 2*p* peaks of all three samples are equally sharp, indicating sharply defined local environments in each, including the amorphous sample. We note that local density approximation (LDA) calculations we have performed predict 0.1–0.3 eV differences in the binding energies of Fe 2*p* core levels due to the two different Fe sites (Fe_I and Fe_{II}). But since these values are comparable with the total experimental resolution (0.23 eV), we do not see any clear splitting in the peaks. Such site-specific effects are more prominent in the valence bands, where the electrons from Fe_I and Fe_{II} have stronger interactions with the different chemical environments of the two lattice sites due to their delocalized nature. We return to discuss this in more detail in the discussion of valence-band spectra.

Figure 4(b) shows the close-lying, and in fact overlapping, Fe 3*s* and Si 2*p* core spectra for all three samples. It is first important to note that the spin-orbit splitting of the Si 2*p* peaks is well-resolved for the epitaxial samples and clearly visible for the amorphous sample (see the inset), indicating that from the standpoint of the chemical environment of the Si atoms, only one type of atomic Si is present in the structure.[33] For the epitaxial films, this is not surprising and is consistent with the ordering observed in x-ray diffraction and CEMS. In both the $D0_3$ and $B2$ crystal structures, Si has only one chemical environment for its nearest neighbors. Only the *next* nearest neighbors differ between the crystal structures, but this difference evidently does not produce a binding - energy shift that is significant with respect to the spin-orbit splitting of 0.59 eV.[33] Therefore, it cannot be detected from the Si 2*p* peak profile in the photoemission spectra. The behavior of the Si 2*p* peak for the amorphous sample is similar to that of the Si 1*s* peak—the position is shifted by 0.27 eV toward lower binding energy relative to the epitaxial sample of the same composition; this is expected in general, since all core levels in a given atom generally show about the same chemical shift. This shift is likely due to the change in lattice constant, since the composition change itself should not cause a substantial change in nearest neighbors, but substantial shifts are seen between the amorphous and crystalline structures of the same composition. The spin-orbit splitting for the amorphous sample is clearly visible, but somewhat broadened and not as well-resolved as that for the epitaxial samples, which reflects a mostly single Si chemical environment in the amorphous sample, despite the absence of long-range order. The Si oxide peak observed at 102.3 eV is higher in intensity compared to both epitaxial samples, consistent with the observation for the Si 1*s* peaks discussed earlier, and attributed to a thicker oxide layer on the amorphous sample.

The Fe 3*s* spectrum in Fig. 4(b) is expected to show multiplet splitting effects, as seen in numerous prior studies of metallic Fe. Many-electron final-state effects of this kind are responsible for the asymmetric nature of the main Fe 3*s* peak and the shoulder seen at ∼96 eV, as well as the broad feature seen ∼115 eV.[34] The behavior of the shoulder with composition suggests qualitatively that there is not a significant change in the Fe magnetic moment as seen in photoemission, even though other measurements indicate the moments to be $1.62\mu_B$, $1.29\mu_B$, and $1.42\mu_B$ for epi-$Fe_{0.72}Si_{0.28}$, epi-$Fe_{0.67}Si_{0.33}$, and *a*-$Fe_{0.67}Si_{0.33}$, respectively.

B. Valence-band spectra

Having examined the core levels, we now look at the near valence-band region, with these results summarized in Figs. 5–7.

As a guide from theory as to which orbital components should be most visible at our photon energy, based on the tabulated values of atomic subshell photoionization cross sections,[35,36] the valence bands of the Fe_xSi_{1-x} alloys [Fig. 5(a)] should be dominated at a 6 keV photon energy by Fe 4*s* states and Si 3*s* states, with the following differential cross-section ratios: Fe 3*d* : Fe 4*s* : Si 3*s* : Si 3*p* : O 2*s* : O 2*p* = 9.1 : 33.5 : 33.0 : 1.6 : 36.6 : 1.3. O 2*s* is also expected

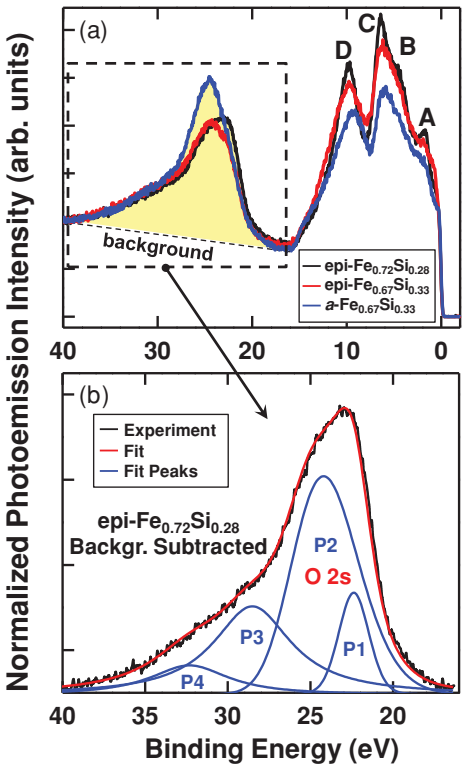

FIG. 5. (Color online) (a) Extended valence-band spectra obtained for all three samples, including the valence-band features labeled *A*–*D* and the subvalence feature, later decomposed into four components (*P*1–*P*4), and normalized to the high-binding-energy inelastic background tail. (b) Higher-binding-energy valence feature, background-subtracted and fitted, with a dominant peak (*P*2) corresponding to the photoemission from O 2*s* levels in the SiO_2 layer.

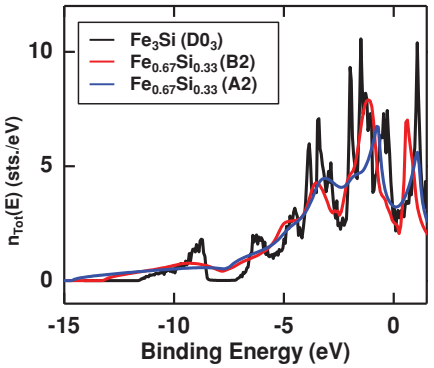

FIG. 6. (Color online) Total calculated densities of states for ordered $D0_3$ Fe_3Si (used as the model for epi-$Fe_{0.72}Si_{0.28}$), partially disordered $FeFe_{0.3}Si_{0.7}$ in the $B2$ structure (epi-$Fe_{0.67}Si_{0.33}$), and for chemically disordered bcc $Fe_{0.67}Si_{0.33}$, used for the amorphous a-$Fe_{0.67}Si_{0.33}$ sample.

to contribute since silicon oxide is present, but generally at a higher binding energy around 20–25 eV based on past studies.[37]

The broad spectra in Fig. 5(a) show that, in addition to the low-binding-energy valence features between 0 and 15 eV, seen in prior XPS measurements on Fe silicides,[19] we find a large peak centered at about 25 eV binding energy. With simple linear background subtraction, the latter feature can be decomposed into four separate peaks shown in Fig. 5(b), centered at 22.5, 24.3, 28.9, and 32.9 eV, but with a dominant peak (labeled $P2$) at 24.3 eV. The intensities of the $P2$ peaks correlate with the higher-binding- energy components of the O 1s peaks (Si oxide peaks) to within 7%. Therefore, we draw the conclusion that the dominant peak ($P2$) in the subvalence feature at 25 eV corresponds to the photoemission from O 2s–dominated levels in the silicon-oxide layer. The other, less prominent peaks comprising this subvalence feature most likely originate from the oxygen-containing solid contaminant layer on the surface, inelastic losses of the valence electrons, and/or hybridization of the O 2s shell with other orbitals in the sample.[37] Furthermore, the observation of the increased relative intensity of this O 2s–dominated subvalence feature

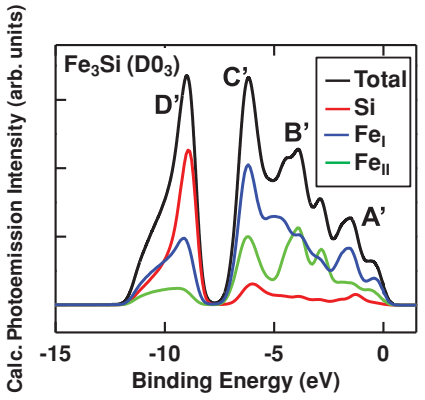

FIG. 7. (Color online) Calculated element- and site-resolved angle-integrated XPS spectra for ordered $D0_3$ Fe_3Si (used to model epi-$Fe_{0.72}Si_{0.28}$) [cf. Fig. 6(a)], including 230 meV broadening due to the total experimental resolution.

for the amorphous sample is consistent with the prior finding of the thicker oxide layer on this sample.

Turning now to the low-binding-energy part of the spectrum, we observe four prominent features, which we label A, B, C, and D, also observed in prior XPS studies,[19,21,38] but at lower excitation energies, and therefore with different relative intensities due to photoelectric cross sections. The spectral feature A at 1.7 eV exhibits a characteristic sharp peak for the epi-$Fe_{0.72}Si_{0.28}$, and has been observed in prior studies of stoichiometric iron silicide, Fe_3Si.[21,38,39] This sharp peak disappears as the Fe/Si ratio deviates from 3/1. The likely origins of these features will be discussed after the theoretical section below.

V. THEORETICAL ANALYSIS AND DISCUSSION

To fully understand the experimental data, we have performed first-principles calculations using the local-spin-density approximation (LSDA) of density functional theory within the spin-polarized fully relativistic Korringa-Kohn-Rostoker Green's function method (SPR-KKR).[40,41] For the exchange and correlation potential, we applied the Vosko, Wilk, and Nusair parametrization.[42] The substitutional disorder has been treated within the coherent-potential approximation (CPA).[43] The CPA is considered to be the best approach among the so-called single-site (local) alloy theories that assume complete random disorder and ignore short-range order. This scheme is implemented within the framework of the above-mentioned SPR-KKR method. As a first step of our theoretical investigation, we performed self-consistent electronic-structure calculations of the total and orbital-projected densities of states for three different compositions of Fe_xSi_{1-x} using the corresponding experimental lattice constant, e.g., for ordered Fe_3Si in the $D0_3$ structure (a = 5.63 Å), for partially disordered $FeFe_{0.3}Si_{0.7}$ in the $B2$ structure (a = 2.79 Å), and for chemically disordered bcc $Fe_{0.67}Si_{0.33}$ (a = 2.79 Å). As a second step, actual valence-band photoemission spectra were calculated using a recent implementation of the fully relativistic CPA formalism in the framework of the one-step model of photoemission, which implicitly includes all matrix elements.[22,23]

The calculated total densities of states are shown in Fig. 6 for three materials: $D0_3$ Fe_3Si, $B2$ $Fe_{0.67}Si_{0.33}$, and $A2$ $Fe_{0.67}Si_{0.33}$. It should be noted here that the epi-$Fe_{0.72}Si_{0.28}$ sample has $D0_3$ structure, but deviates from the perfectly ordered Fe_3Si compound used in the model because of being off-stoichiometry, and the $A2$ structure (random bcc solid solution) is used as an approximation for the amorphous sample. The sharp features observed in the densities of states (DOS) of the ordered Fe_3Si are smeared out by chemical disorder in the $B2$ and $A2$ structures, which is an expected result of introducing disorder. In particular, this broadening is clearly visible for the peak labeled D, which is located at about 10 eV binding energy, and which via projected densities of states is found to be mostly due to Si 3s. With increasing disorder (first compositional, then structural), this Si 3s peak in the total DOS is significantly broadened, with its spectral weight shifted to higher binding energies. The effects of disorder-induced broadening are also seen in other density of states features (peaks A–C at about 1, 2, and 4 eV binding energy). It is also

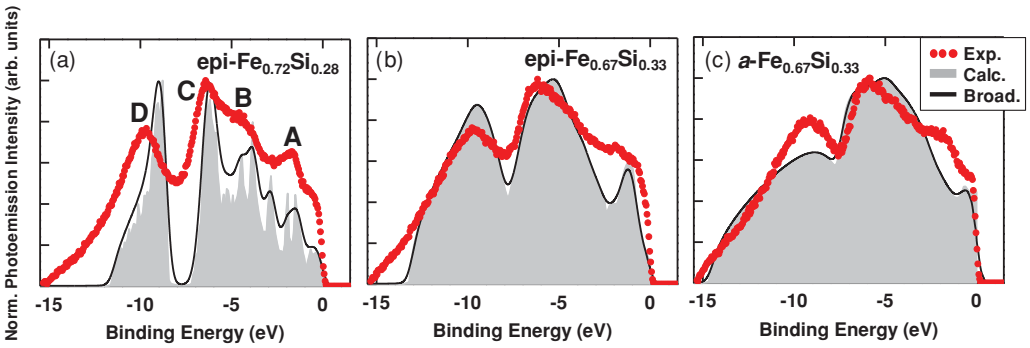

FIG. 8. (Color online) Room-temperature XPS spectra for (a) ordered $D0_3$ Fe_3Si (used to model epi-$Fe_{0.72}Si_{0.28}$), (b) partially disordered $FeFe_{0.3}Si_{0.7}$ in the $B2$ structure (used to model epi-$Fe_{0.67}Si_{0.33}$), and (c) chemically disordered bcc a-$Fe_{0.67}Si_{0.33}$ at a photon energy of 5950.3 eV compared to calculated one-step theoretical spectra shown in gray. The black curves represent a broadening of the theoretical spectra with a 230 meV (FWHM) Gaussian to simulate the experimental resolution. Experimental data, normalized to the high-binding-energy inelastic background tail, are shown in red.

noteworthy that the shift of the Si 3*s* feature (peak *D*) toward higher binding energies is similar in direction and value to the chemical shift we observed for the elemental Si 1*s* and Si 2*p* core peaks (see Fig. 3).

For photon energies in this hard x-ray regime, and as noted above, we expect on the basis of atomic subshell photoionization cross sections[35] that the intensity distribution will be dominated by transitions involving initial states of Fe with *sp*-like angular momentum character. For this reason, it is necessary to perform complete photoemission calculations including all matrix element effects and not to restrict the analysis to a comparison between the calculated DOS and the experimental XPS spectra. To clarify the various orbital contributions to the experimental spectra via such calculations, we show in Fig. 7 element- and site-resolved photoemission spectra of ordered Fe_3Si, calculated within the one-step model. The calculated KKR electronic-structure wave-functions were used in this calculation, and all matrix element effects were included. We see features A'–D', much like in the experimental spectra. We also see that feature A' is dominated by Fe_I, feature B' is dominated by Fe_{II}, feature C' is about 2/3 Fe_I and 1/3 Fe_{II}, and feature D' is dominated by Si. Comparing these results to data in Fig. 5(a), the decreased intensity of peaks *A* and *C* between the two epitaxial samples is associated with the decrease in Fe_I atoms due to Si substitution. Fe_I dominates the features close to the Fermi level (*A*, *B*, and *C*), and these features can further be identified with the *sp*-like DOS of Fe_I (not shown here). Due to strong hybridization of the Fe *sp*-like states with the Fe 3*d* states, the changes in the observed spectral intensities of the *sp* states, which dominate the valence-band spectra due to their high photoionization cross sections, can be directly related to the behavior of the Fe 3*d* states.

Finally, in Fig. 8, we compare our experimental valence spectra for the three materials to angle-integrated valence-band photoemission calculations at a photon energy of 5950.3 eV, again with all matrix-element effects included. Because the energy and temperature are high, angle integration to achieve the so-called XPS limit is appropriate.[44] Good agreement with the experimental data is obtained in Fig. 8, especially for the epi-$Fe_{0.67}Si_{0.33}$ and a-$Fe_{0.67}Si_{0.33}$ samples, for which most features are correctly predicted as to position, width, and relative intensity. All features *A*–*D* for epi-$Fe_{0.72}Si_{0.28}$ are also predicted, but peak *D* (due to the Si 3*s* states) is predicted to be at lower binding energy (by about 1 eV), most likely due to the fact that the epi-$Fe_{0.72}Si_{0.28}$ was modeled as a perfectly ordered $D0_3$ structure, while in reality it has a $D0_3$ structure with extra Si in preferential substitution at the Fe_I site because the sample is more Si-rich than the stoichiometric Fe_3Si compound. Moreover, the calculated spectrum exhibits much sharper features than the experimental one, which is also due to the disorder broadening due to the excess Si of epi-$Fe_{0.72}Si_{0.28}$ compared to the perfectly ordered Fe_3Si compound that is used to obtain the calculated spectrum.

When comparing the three samples, it appears the calculations overestimate the features connected with the 3*s* states of Si (feature *D*) for the two epitaxial samples, whereas for the amorphous sample this feature is underestimated. The behavior of feature *D* for the amorphous sample is similar to that of the Si 1*s* and Si 2*p* peaks—the position is shifted by 0.45 eV toward lower binding energy relative to the epitaxial sample of the same composition. This shift is due to a difference in chemical environment around the Si atoms in the amorphous structure compared to the crystalline structures ($D0_3$ and $B2$). Perhaps even more remarkably, the *D* (Si) peak for the amorphous sample is sharper than that for the calculated random crystalline ($A2$) alloy, suggesting that the amorphous structure possesses on average a better defined local structure around the Si atoms than a random alloy. Also, the amorphous sample shows a clear sign of an *A* peak, not seen in the random alloy calculations. Better modeling of the amorphous structure is required to say more. Despite some minor discrepancies, one can conclude that these one-step photoemission calculations provide a good qualitative description of the data. Combining this type of analysis with spin resolution, as is now planned in a couple of facilities, should enable characterizing and tailoring such materials in a much more precise way for future spintronic applications.

VI. SUMMARY

We have investigated the structural and electronic properties of near-Heusler epitaxial and amorphous Fe_xSi_{1-x} alloys with

$x = 0.72$ and 0.67 using hard x-ray photoelectron spectroscopy. With a photon energy of 5950.3 eV, we ensure that the inelastic mean-free path of the photoemitted electrons is large enough (~76 Å) so that we probe deep into the bulk of the solid, with an average emission depth of about 13 unit cells into the sample. Binding-energy shifts in Si 1*s* and 2*p* peaks suggest changes in the chemical environment around the Si atoms in the alloys of different compositions and structural orderings. This shift is likely due to the change in lattice constant, since the composition change itself should not cause a substantial change in nearest neighbors, but substantial shifts are seen between the amorphous and crystalline structures of the same composition. Remarkably, the peaks in the amorphous structure shows little broadening despite a significant energy shift, suggesting that the local environment around the Si atoms is different from that in the crystalline materials but far more uniform than might have been expected. Similar but smaller in magnitude shifts, and a similar lack of broadening in the amorphous sample, are seen in the Fe 2*p* peaks. Analysis of the Si 1*s* oxide satellite and O 1*s* peaks revealed that the surface is oxidized to thicknesses of about 10.4–13.5 Å for the epitaxial samples and 26.2–32.4 Å for the amorphous sample. Analysis of the Fe 2*p* peaks shows that Fe is in the Fe^0 state without significant signs of oxidation. Analysis of the C 1*s* and O 1*s* core peaks also revealed the presence of a thin (9.4–10.5 Å) carbon- and oxygen-containing atmospheric contaminant on the surfaces of the samples, above the Si oxide layer. A well-resolved Si 2*p* spin-orbit splitting for the two epitaxial alloys suggests that nearest-neighbor interactions are the dominant effect on binding energy for the Si atoms in the sample. The Si 2*p* peak also shows spin-orbit splitting for the amorphous sample, another indication that the local structure around each Si atom is relatively well defined. In the valence-band region, investigation of a prominent feature centered at about 25 eV below the Fermi level revealed that it arises mostly due to photoemission from O 2*s* levels in the surface Si oxide layer. Analysis of the other valence bands, which are expected to be dominated by Si 3*s* states and Fe *sp* states (but which are strongly hybridized with Fe 3*d* states), shows a broadening of the features when chemical and structural disorder is increased. Distinctly different contributions from the two inequivalent Fe sites in the valence-band spectrum of the most highly ordered ($D0_3$) epitaxial sample are observed. These features are reduced but not completely eliminated in the *B*2 sample and most remarkably for the amorphous sample. Lastly, CPA calculations of the valence-band photoemission spectra have been performed and show good agreement with the experimental spectra, thus confirming the origin of the observed features and revealing the more important contribution of the Fe_I site to the spectra.

ACKNOWLEDGMENTS

Research was supported by the U.S. Department of Energy, Office of Science, Office of Basic Energy Sciences, Division of Materials Sciences and Engineering under Contract No. DE-AC02-05CH11231 (A.X.G., J.K., C.B., F.H., and C.S.F.), by the Nanotechnology Network Project, the Ministry of Education, Culture, Sports, Science and Technology (MEXT), Japan (S.U., Y.Y., and K.K.), and by Deutsche Forschungsgemeinschaft under Projects EBE-154/18, EBE-154/20, and MI-1327/1 (J.M., H.E., and J.B.).

[1] J. Herfort, H.-P. Schönherr, A. Kawaharazuka, M. Ramsteiner, and K. H. Ploog, J. Cryst. Growth **278**, 666 (2005).
[2] Y. Ando, K. Hamaya, K. Kasahara, Y. Kishi, K. Ueda, K. Sawano, T. Sadoh, and M. Miyao, Appl. Phys. Lett. **94**, 182105 (2009).
[3] T. J. Burch, T. Litrenta, and J. I. Budnick, Phys. Rev. Lett. **33**, 421 (1974).
[4] R. A. de Groot, F. M. Mueller, P. G. van Engen, and K. H. J. Buschow, Phys. Rev. Lett. **50**, 2024 (1983).
[5] J. Kudrnovský, N. E. Christensen, and O. K. Andersen, Phys. Rev. B **43**, 5924 (1991).
[6] A. Ionescu, C. A. F. Vaz, T. Trypiniotis, C. M. Gürtler, H. García-Miquel, J. A. C. Bland, M. E. Vickers, R. M. Dalgliesh, S. Langridge, Y. Bugoslavsky, Y. Miyoshi, L. F. Cohen, and K. R. A. Ziebeck, Phys. Rev. B **71**, 094401 (2005).
[7] T. Yoshitake, D. Nakagauchi, T. Ogawa, M. Itakura, N. Kuwano, Y. Tomokiyo, T. Kajiwara, and K. Nagayama, Appl. Phys. Lett. **86**, 262505 (2005).
[8] B. Jenichen, V. M. Kaganer, J. Herfort, D. K. Satapathy, H. P. Schönherr, W. Braun, and K. H. Ploog, Phys. Rev. B **72**, 075329 (2005).
[9] B. Krumme, C. Weis, H. C. Herper, F. Stromberg, C. Antoniak, A. Warland, E. Schuster, P. Srivastava, M. Walterfang, K. Fauth, J. Minár, H. Ebert, P. Entel, W. Keune, and H. Wende, Phys. Rev. B **80**, 144403 (2009).
[10] K. Zakeri, S. J. Hashemifar, J. Lindner, I. Barsukov, R. Meckenstock, P. Kratzer, Z. Frait, and M. Farle, Phys. Rev. B **77**, 104430 (2008).
[11] K. Trunov, M. Walterfang, W. Keune, N. K. Utochkina, and A. Trunova, Thin Solid Films **516**, 6205 (2008).
[12] W. A. Hines, A. H. Menotti, J. I. Budnick, T. J. Burch, T. Litrenta, V. Niculescu, and K. Raj, Phys. Rev. B **13**, 4060 (1976).
[13] D. Berling, G. Gewinner, M. C. Hanf, K. Hricovini, S. Hong, B. Loegel, A. Mehdaoui, C. Pirri, M. H. Tuilier, and P. Wetzel, J. Magn. Magn. Mater. **191**, 331 (1999).
[14] W. H. Wang, M. Przybylski, W. Kuch, L. I. Chelaru, J. Wang, Y. F. Lu, J. Barthel, H. L. Meyerheim, and J. Kirschner, Phys. Rev. B **71**, 144416 (2005).
[15] M. V. Yablonskikh, J. Braun, M. T. Kuchel, A. V. Postnikov, J. D. Denlinger, E. I. Shreder, Y. M. Yarmoshenko, M. Neumann, and A. Moewes, Phys. Rev. B **74**, 085103 (2006).
[16] H. Miyazaki, K. Soda, S. Yagi, M. Kato, T. Takeuchi, U. Mizutani, and Y. Nishino, J. Vac. Sci. Technol. A **24**, 1464 (2006).
[17] C. J. Powell, A. Jablonski, I. S. Tilinin, S. Tanuma, and D. R. Penn, J. Electron Spectrosc. Relat. Phenom. **98**, 1 (1999).
[18] S. Tanuma, C. J. Powell, and D. R. Penn, Surf. Interface Anal. **37**, 1 (2005).
[19] B. Egert and G. Panzner, Phys. Rev. B **29**, 2091 (1984).

[20]J. Alvarez, J. J. Hinarejos, E. G. Michel, J. M. Gallego, A. L. Vazquez de Parga, J. de la Figuera, C. Ocal, and R. Miranda, Appl. Phys. Lett. **59**, 99 (1991).
[21]I. N. Shabanova, V. I. Kormilets, and N. S. Terebova, J. Electron Spectrosc. Relat. Phenom. **114**, 609 (2001).
[22]J. Braun, J. Minár, F. Matthes, C. M. Schneider, and H. Ebert, Phys. Rev. B **82**, 024411 (2010).
[23]H. Ebert and J. Schwitalla, Phys. Rev. B **55**, 3100 (1997).
[24]B. L. Henke, E. M. Gullikson, and J. C. Davis, At. Data Nucl. Data Tables **54**, 181 (1993).
[25]D. A. Shirley, Phys. Rev. B **5**, 4709 (1972).
[26]F. J. Himpsel, F. R. McFeely, A. Taleb-Ibrahimi, J. A. Yarmoff, and G. Hollinger, Phys. Rev. B **38**, 6084 (1988).
[27]J. M. Hill, D. G. Royce, C. S. Fadley, L. F. Wagner, and F. J. Grunthaner, Chem. Phys. Lett. **44**, 225 (1976).
[28]R. L. Opila, Appl. Surf. Sci. **256**, 1313 (2009).
[29]W. Smekal, W. S. M. Werner, and C. J. Powell, Surf. Interface Anal. **37**, 1059 (2005).
[30]S. J. Roosendaal, B. van Asselen, J. W. Elsenaar, A. M. Vredenberg, and F. H. P. M. Habraken, Surf. Sci. **442**, 329 (1999).
[31]O. Kubashewski, E. Evans, and S. B. Alcock, *Metallurgical Thermochemistry*, 4th ed. (Pergamon, Oxford, 1967).
[32]C. S. Fadley, S. B. M. Hagstrom, M. P. Klein, and D. A. Shirley, J. Chem. Phys. **48**, 3779 (1968).
[33]E. Landemark, C. J. Karlsson, Y.-C. Chao, and R. I. G. Uhrberg, Phys. Rev. Lett. **69**, 1588 (1992).
[34]C. S. Fadley and D. A. Shirley, Phys. Rev. A **2**, 1109 (1970).
[35]J. H. Scofield, Tech. Rep. UCRL-51326, LLNL (1973).
[36]M. Oku, T. Shishido, H. Matsuta, and K. Wagatsuma, J. Electron Spectrosc. Relat. Phenom. **153**, 75 (2006).
[37]V. P. Zakaznova-Herzog, H. W. Nesbitt, G. M. Bancroft, J. S. Tse, X. Gao, and W. Skinner, Phys. Rev. B **72**, 205113 (2005).
[38]I. N. Shabanova, N. S. Terebova, and V. I. Kormilets, Phys. Solid State **42**, 1196 (2000).
[39]Y. T. Cui, A. Kimura, K. Miyamoto, K. Sakamoto, T. Xie, S. Qiao, M. Nakatake, K. Shimada, M. Taniguchi, S.-I. Fujimori, Y. Saitoh, K. Kobayashi, T. Kanomata, and O. Nashima, Phys. Status Solidi A **203**, 2765 (2006).
[40]H. Ebert *et al.*, The Munich SPR-KKR package, version 5.4 [http://olymp.cup.uni-muenchen.de/ak/ebert/SPRKKR] (2009).
[41]H. Ebert, in *Electronic Structure and Physical Properties of Solids*, edited by H. Dreyssé, Lecture Notes in Physics, Vol. 535 (Springer, Berlin, 2000), p. 191.
[42]S. H. Vosko, L. Wilk, and M. Nusair, Can. J. Phys. **58**, 1200 (1980).
[43]J. S. Faulkner and G. M. Stocks, Phys. Rev. B **21**, 3222 (1980).
[44]C. S. Fadley, J. Electron Spectrosc. Relat. Phenom. **178**, 2 (2010).